# Reaching the quantum limit of sensitivity in electron spin resonance

A. Bienfait, J. Pla, Y. Kubo, M. Stern, X. Zhou, C.C. Lo, C.D. Weis, T. Schenkel, M.L.W. Thewalt, D. Vion, D. Esteve, B. Julsgaard, K. Mølmer, J.J.L. Morton, and P. Bertet

I. EXPERIMENTAL DETAILS

Bismuth implanted sample

The sample consists of a natural silicon (100) substrate on which a $700\,$nm-thick isotopically enriched 99.95% ^{28}Si epitaxial layer was grown. Bismuth dopants were subsequently implanted into the epitaxial layer and activated by thermal annealing (see [1] for more details). The implantation profile, measured via Secondary Ion Mass Spectroscopy (SIMS) is shown in 1 of the main text. The activation step consists in an anneal to $800°C$ for $20\,$min under nitrogen atmosphere. An electrical activation yield of 60% has been measured using a Hall effect measurement system under similar implantation conditions [1].
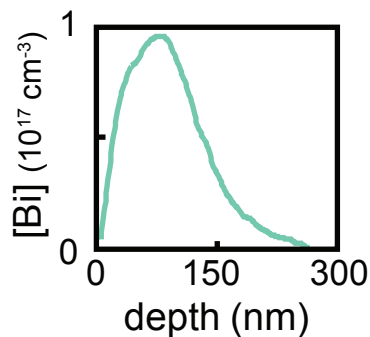
Supplementary Fig. 1. Bismuth implantation profile, measured via Secondary Ion Mass Spectroscopy (SIMS)

A 50-nm-thick aluminum resonator was deposited on top of the sample using a standard lift-off process. The resonator is a lumped element constituted by a 5μm-wide wire and an interdigitated capacitance of 12 50μm-wide fingers spaced by $50\,\mu$m. The wire is $730\,\mu$m long yielding a resonance $\omega_0/2\pi = 7.26\,$GHz.
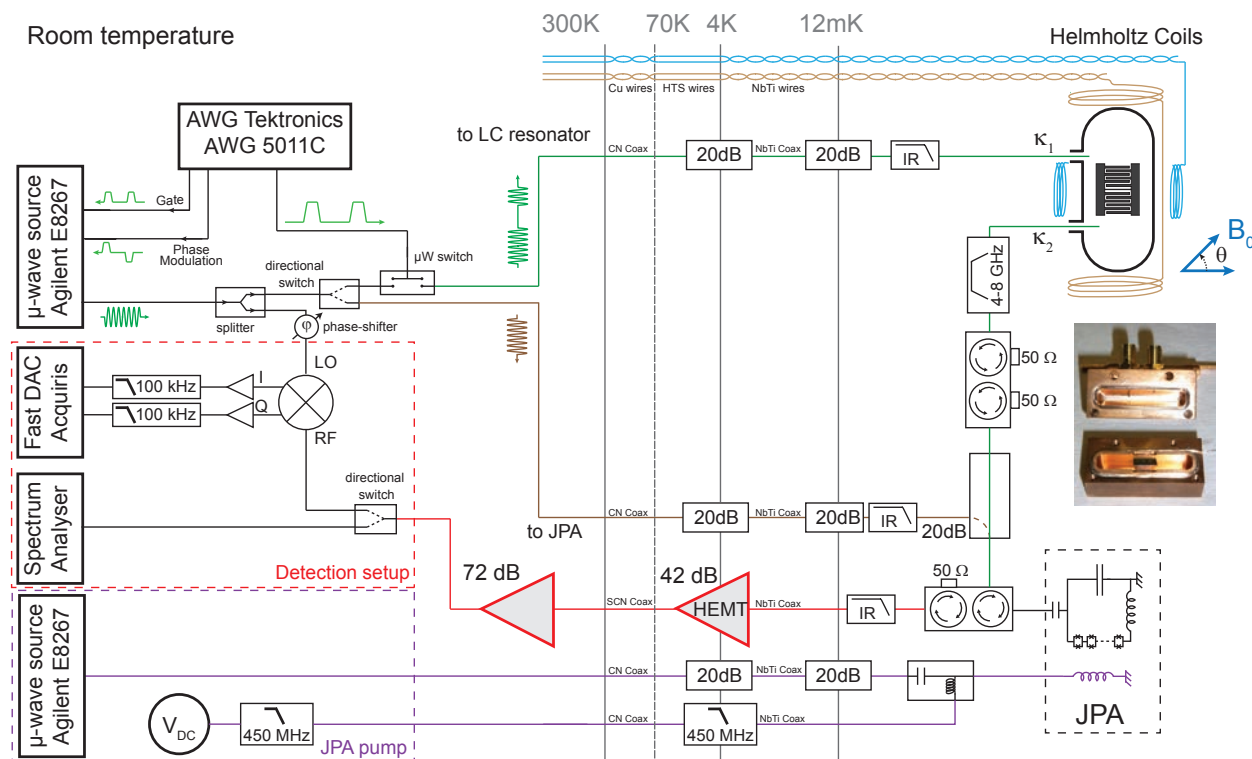
Measurement setup

The detailed microwave setup is shown in supplementary Fig. 2. The sample is enclosed in a box made of oxygen-free-high-conductivity-copper, whose lowest resonance mode is at 8.4 GHz. Its role is to suppress the resonator radiative losses, while enabling its coupling to the input and output antennas with rates κ_1 (input) and κ_2 (output). The values of κ_1 and κ_2 as well as the resonator internal losses κ_L are determined experimentally by measuring the complete resonator scattering matrix with the spins far from resonance, and fitting this matrix to the known resonator input-output formulas (see [2] for instance). The results are shown in Table I. As can be seen in Table I, the experiment is in the so-called critical coupling regime where the internal losses κ_L are approximately equal to the external coupling $\kappa_1 + \kappa_2$. The asymmetry between κ_1 and κ_2 was purposely chosen to be large (≈ 5) so as to ensure that the majority of the photons emitted by the spins would be collected by the output antenna. The resonator total quality factor is $Q = \dfrac{\omega_0}{\kappa_1 + \kappa_2 + \kappa_L} = 3 \times 10^5$.

$\frac{\omega_r}{2\pi}$	Q	κ_1	κ_2	κ_L
7.24 GHz	3×10^5	$1.3 \times 10^4 \, \mathrm{s}^{-1}$	$5.8 \times 10^4 \, \mathrm{s}^{-1}$	$7.5 \times 10^4 \, \mathrm{s}^{-1}$

Supplementary Table I.

During a spin-echo sequence, a series of microwave pulses at frequency ω_0 is sent on the input line of the cavity (κ_1, green wire on the figure). The transmitted signal is then routed to the Josephson Parametric Amplifier (JPA) via a circulator and is further amplified first by a low-noise HEMT amplifier at the 4K stage then at room temperature, before being finally demodulated by mixing with the local oscillator at frequency ω_0.

The JPA can be studied and tuned independently from the cavity by an additional input line (brown) coupled via a 20dB coupler to the cavity output line. Its design and operation have been described in detail in [3]. It consists of a lumped element resonator formed by an interdigitated capacitance, a geometrical inductance and an array series of 8 superconducting quantum interference devices (SQUIDs). The SQUID array acts as a flux-tunable inductor that allows the resonator frequency to be tuned over a 400 MHz frequency range by passing a dc current through an on-chip antenna. The amplifier is parametrically pumped by modulating the flux threading the SQUIDs at a frequency ω_p close to twice the resonator frequency. The JPA can be operated either in phase sensitive mode where

Supplementary Fig. 2. Measurement setup.

$\omega_p/2 = \omega_0$ or in non-degenerate mode. In the latter mode, around $7.3\,\text{GHz}$, a non-degenerate gain of $23\,\text{dB}$ can be obtained with the appropriate pump power as shown in Fig. 1 of the main text. Saturation of the JPA occurs for a typical input power of $-130\,\text{dBm}$. In all the data presented in this work, the echo signals emitted by the spins are below the amplifier saturation threshold. The detuning between the pump and the signal is chosen to be $\approx 500\,\text{kHz}$, and the demolutated signal is filtered at $100\,\text{kHz}$ to suppress the idler. In phase-sensitive mode, only one signal quadrature is amplified, and the JPA has an additional $6\,\text{dB}$ gain. The quadrature is chosen by tuning the relative phase of the pump and signal sources. In addition, the JPA pump is pulsed via the microwave source internal switch (not shown on schematic) so as to generate gain only during the emission of an echo signal. This is done to reduce the effective pump power brought to the mixing chamber plate and thus bring the cryostat temperature from $20\,\text{mK}$ with a continuous pump signal to $12\,\text{mK}$.

A double circulator is used to prevent interferences between the cavity and the JPA. Another double circulator is needed at the JPA output to ensure both the routing of the signal and the isolation from the thermal photons travelling down the output line (red line).

Leakage of the $14.5\,\mathrm{GHz}$ pump to the resonator and the spins is suppressed by a $4-8\,\mathrm{GHz}$ bandpass filter inserted between the cavity and the JPA. Each input line is attenuated by 20dB at 4K and 20dB at 12mK to thermalize the electromagnetic field, and filtered by low-pass filters containing infra-red absorptive material in order to minimize losses due to out-of-equilibrium quasi-particles generated in the superconducting thin-film. Both the cavity and the JPA are magnetically shielded. The JPA is enclosed in a 3-cm-wide aluminium box surrounded by a 1-mm-thick cryoperm material, the whole being placed inside a 20-cm-long μ-metal cylindrical shield. The magnetic field B_0 is applied parallel to the sample surface with an arbitrary angle θ with respect to the resonator axis, by using two orthogonal Helmholtz coil pairs that can provide up to $10\,\mathrm{mT}$ and have been calibrated in a previous experiment.

Pulses are shaped by a microwave switch in series with the microwave source internal gate. The relative phases of the pulses are controlled by analog phase modulation. Every control signal is generated by an arbitrary wavefrom generator (AWG). In order to suppress any offset in the detection chain without time-consuming calibration, every pulse sequence is repeated twice with opposite phases on the $\pi/2$ pulses. This phase cycling protocol yields two echo signals with opposite phases taken in the same conditions : the offset is removed by taking the difference between the two time traces acquired on each sequence.

The duration of the control pulses in our spin-echo sequences (respectively 2.5μs and 2.5μs for the $\pi/2$ and π pulses) is much shorter than the time $\tau = 2/\kappa = 14\mu$s after which the intra-resonator field reaches steady-state. As a result, the field amplitude starts by rising linearly in time during the pulse duration, after what it decays exponentially with time constant τ, giving rise to the asymmetric pulse profile that can be seen in Fig.3c of the main text in the transmitted microwave signal amplitude. Correspondingly, the spin Rabi frequency $\Omega_R(t)$ follows the same time-dependence, reaching a maximum frequency $\Omega_{R,max}$ at the end of the pulse before decaying exponentially. The integrated Rabi angle over the pulse duration being approximately given by $2\Omega_{R,max}/\kappa$, one sees that $\Omega_{R,max} \approx \kappa\pi/4$ for the $\pi/2$ pulse and $\kappa\pi/2$ for the π pulse. This indicates that spins whose frequency lies within the cavity bandwidth and therefore contribute to the echo signal are indeed driven by the control pulses and efficiently refocused by the π pulse, even though there remains a slight dependence of the exact trajectory they perform on the Bloch sphere on their detuning to the resonator frequency. In future experiments, more complex shaping of the control pulses

could probably reduce this source of inhomogeneity. In the present experiment it is however not detrimental as evidenced by the well-defined Rabi oscillations shown in Fig.2b of the main text.

The spin energy relaxation time T_1 being $\sim 0.4\,\mathrm{s}$ (see Fig.2e of the main text), we choose a repetition rate γ_{rep} sufficiently slow to allow full relaxation of the spins in-between successive sequences. All the data related to the setup sensitivity (Figure 3a and Figure 4) have been taken with a repetition rate of $\gamma_{rep} = 1\,\mathrm{Hz}$. For other measurements, the repetition rate was chosen slightly slower: the spin-echo spectroscopy shown in Figure 2 is acquired with $\gamma_{rep} = 0.04\,\mathrm{Hz}$, the data of Figure 3a&c with $\gamma_{rep} = 0.1\,\mathrm{Hz}$ and the absorption data of Figure 3b with $\gamma_{rep} = 0.3\,\mathrm{Hz}$.

II.   BISMUTH DONOR SPIN AND COUPLING TO THE RESONATOR

Neutral bismuth donors in silicon have a $S = 1/2$ electron spin and a nuclear spin $I = 9/2$ that are strongly coupled by an isotropic hyperfine interaction term $A/2\pi = 1.45$ GHz. The system is described with the following Hamiltonian, [4], where $\gamma_e/2\pi = 28$ GHz/T and $\gamma_n/2\pi = 7$ MHz/T :

$$\hat{H}/\hbar = \mathbf{B} \cdot (\gamma_e \mathbf{S} \otimes \mathbb{1} - \gamma_n \mathbb{1} \otimes \mathbf{I}) + A\,\mathbf{S} \cdot \mathbf{I} \tag{1}$$

In the limit of low static magnetic field B_0, the 20 electro-nuclear energy states are well approximated by eigenstates of the total angular momentum $\mathbf{F} = \mathbf{S} + \mathbf{I}$, which can be grouped in an $F = 4$ ground and an $F = 5$ excited multiplet separated by a frequency of $5A/2\pi = 7.38\,\mathrm{GHz}$ in zero-field, shown on Figure 1. For a given low static field B_0 oriented along $\mathbf{z}$, only transitions verifying $|\Delta m_F| = 1$ have a sizeable S_x matrix element (equals to the S_y matrix element) and so may be probed with an excitation field orientated along $\mathbf{x}$ (or equivalently along $\mathbf{y}$). We give in the table below details on the two transitions that are accessible to our resonator.

Transition	Expected crossing field	df/dB	$\left|\left\langle m_F \mid \hat{S}_x \mid m'_F \right\rangle\right| = \left|\left\langle m_F \mid \hat{S}_y \mid m'_F \right\rangle\right|$
$m_F = -4 \to -5$	$5.16\,\mathrm{mT}$	$-25.1\,\mathrm{GHz/T}$	0.47
$m_F = -3 \to -4$	$6.68\,\mathrm{mT}$	$-19.2\,\mathrm{GHz/T}$	0.42

Supplementary Table II.

Single-spin coupling to the resonator

In the experiment, the static magnetic field B_0 is applied parallel to the surface (see Fig. 2) along an axis $\mathbf{Z}$ that can be decomposed along the orientations defined in Fig. 3 as :

$$\mathbf{B_0} = B_0 \mathbf{Z} = B_0 \cos(\theta)\mathbf{z} + B_0 \sin(\theta)\mathbf{x}. \tag{2}$$

A full orthonormal basis is provided by the combination of $\mathbf{X}, \mathbf{Y}, \mathbf{Z}$, with $\mathbf{X} = \cos\theta\,\mathbf{x} - \sin\theta\,\mathbf{z}$, and $\mathbf{Y} = \mathbf{y}$. The total magnetic field $\mathbf{B}$ is the sum of the static bias magnetic field $\mathbf{B_0}$ and of the microwave field generated by the resonator $\mathbf{B_1} = \delta\mathbf{B}(\hat{a} + \hat{a}^\dagger)$, where we introduce the magnetic field rms fluctuations at the spin location $\delta\mathbf{B}$ and the resonator annihilation (resp. creation) operator $\hat{a}$ (resp. $\hat{a}^\dagger$). The field $\mathbf{B_1}$ is located in the plane perpendicular to the resonator wire; as a result one can write $\delta\mathbf{B} = \delta B_x\mathbf{x} + \delta B_y\mathbf{y} = \delta B_X\mathbf{X} + \delta B_Y\mathbf{Y} + \delta B_Z\mathbf{Z}$, with $\delta B_X = \cos\theta\delta B_x$, $\delta B_Y = \delta B_y$ and $\delta B_Z = \sin\theta\delta B_x$.

Projecting the total Hamiltonian of a single Bismuth donor in the field $\mathbf{B}$ on the Hilbert space spanned by the two levels $|m_F\rangle, |m'_F\rangle$ and introducing the usual Pauli operators yields

$$H/\hbar = \omega_0\hat{a}^\dagger\hat{a} - \frac{\omega_s}{2}\hat{\sigma}_z$$
$$+\gamma_e\left[\langle m_F|S_X\delta B_X + S_Y\delta B_Y + S_Z\delta B_Z|m'_F\rangle\hat{\sigma}_+ + \langle m'_F|S_X\delta B_X + S_Y\delta B_Y + S_Z\delta B_Z|m_F\rangle\hat{\sigma}_-\right](\hat{a}+\hat{a}^\dagger). \tag{3}$$

(In this equation we left aside the $\sigma_z(\hat{a} + \hat{a}^\dagger)$ terms as they contribute only as negligible fast-rotating terms). Here we focus exclusively on transitions $\Delta m_F = -1$ for which $\langle m_F|S_Z|m'_F\rangle = 0$. As noted in the previous paragraph, $\langle m_F|S_X\delta B_X + S_Y\delta B_Y|m'_F\rangle = \langle m_F|S_X|m'_F\rangle(\delta B_X + i\delta B_Y)$, where $\langle m_F|S_X|m'_F\rangle$ values are shown in Table II (≈ 0.5). After performing the rotating-wave approximation, the full system Hamiltonian takes the Jaynes-Cummings form

$$H/\hbar = \omega_0\hat{a}^\dagger\hat{a} - \frac{\omega_s}{2}\hat{\sigma}_z + g(\mathrm{e}^{i\phi_0}\hat{\sigma}_+\hat{a} + \mathrm{e}^{-i\phi_0}\hat{\sigma}_-\hat{a}^\dagger), \tag{4}$$

where ϕ_0 is an irrelevant phase that can be absorbed by a re-definition of the energy levels, and g is the spin-resonator coupling constant given by

$$g = \langle m_F|S_X|m'_F\rangle\gamma_e\sqrt{\delta B_y^2 + (\cos\theta)^2\delta B_x^2}. \tag{5}$$
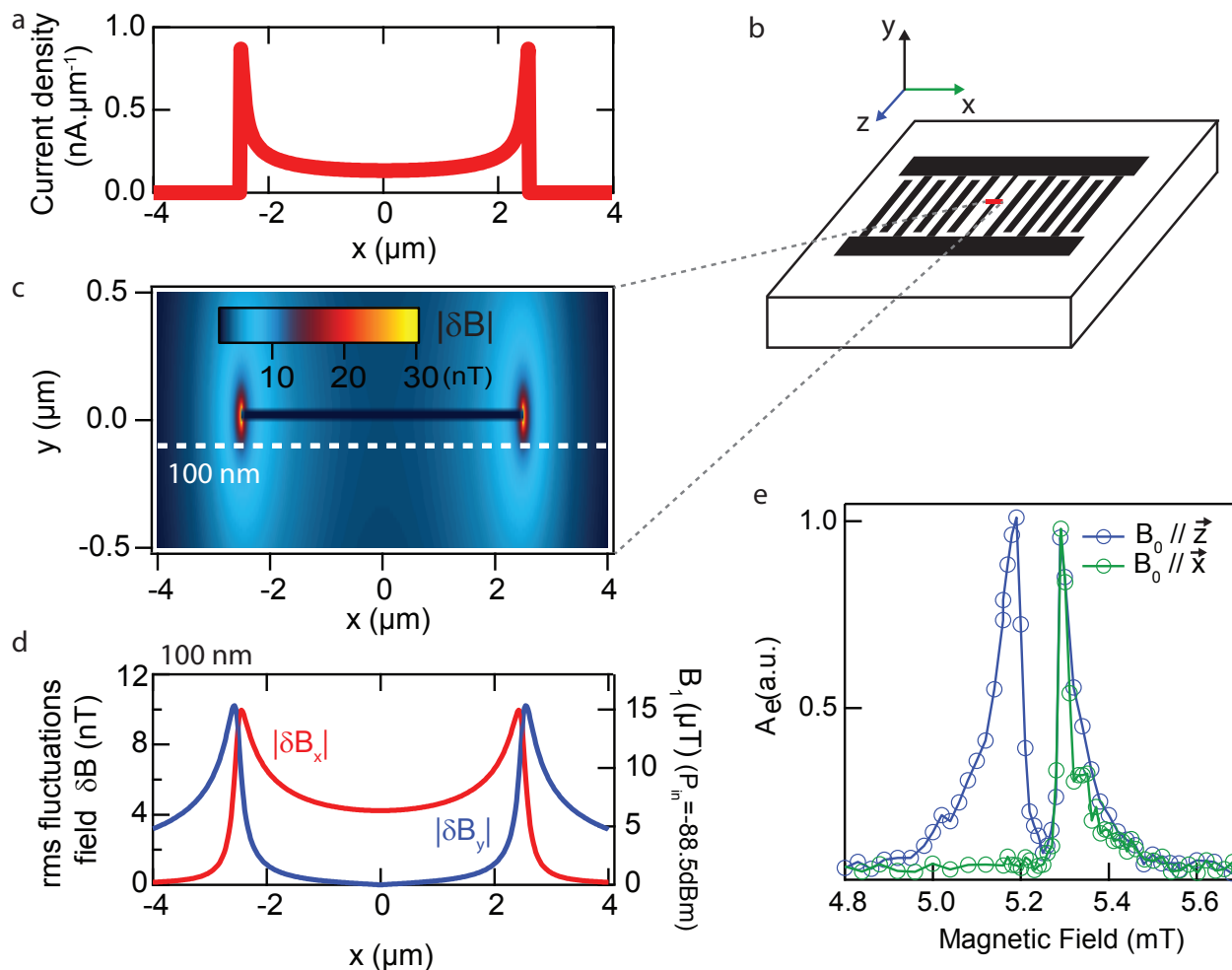
Supplementary Fig. 3. (a) Spatial distribution of the current rms vacuum fluctuations flowing through the resonator inductance, corresponding to an impedance of $44\,\Omega$. (b) Scheme of the resonator, with corresponding directions used in the text. (c) rms vacuum fluctuations of the magnetic field at the given red cross-section on b (d) x (red) and y (blue) components for the vacuum fluctuations of the magnetic field at $y = -100\,\mathrm{nm}$ (left axis) and for the microwave field B_1 corresponding to an input power $P_{in} = -88.5\,\mathrm{dBm} = 1.4\,\mathrm{pW}$ (right axis). (e) Spin-echo spectroscopy realized for $\mathbf{B_0} = B_0 \cdot \mathbf{z}$ (blue circles) and $\mathbf{B_0} = B_0 \cdot \mathbf{x}$ (green circles) allowing to make the distinction between spins lying next (strong δB_y) and under (strong δB_x) the aluminium wire.

The vacuum field fluctuations $\delta \mathbf{B}$ have a spatial dependence, fixed by the shape of the LC resonator mode, which implies that the coupling constant to the resonator will also follow the same spatial dependence. We determine this spatial dependence numerically in the

following way. First, the spatial distribution of the current fluctuations in the resonator wire is computed, knowing that the integrated current over the wire cross-sectional area is given by $\delta i = \omega_0 \sqrt{\hbar/2Z_0}$, $Z_0 = \sqrt{L/C}$ being the resonator impedance estimated to be 44Ω using the electromagnetic simulator CST Microwave Studio. For our $50\,\mathrm{nm}$-thick aluminum films, the current density is assumed constant in the y direction with an x-dependent integrated value $\delta J(x)$ given by [5]:

$$\delta J(x) = \begin{cases} \delta J(0)[1 - (2x/w)^2]^{-1/2} & \text{for } |x| \leq |\tfrac{1}{2}w - \lambda^2/(2b)| \\ \delta J(\tfrac{1}{2}w) \exp - \left[\left(\tfrac{1}{2}w - |x|\right) b/\lambda^2\right] & \text{for } |\tfrac{1}{2}w - \lambda^2/(2b)| < |x| < \tfrac{1}{2}w \\ (1.165/\lambda)(wb)^{1/2}\delta J(0) & \text{for } x = \tfrac{1}{2}w. \end{cases} \quad (6)$$

In these expressions, $w = 5\ \mu$m is the width of the wire, $b = 50$ nm is its thickness and $\lambda = 90$ nm is the penetration depth for our Al film. The normalization constant $\delta J(0)$ is determined by the condition that $\int_{-w/2}^{w/2} \delta J(x)dx = \delta i$. From the current distribution, the spatial dependence of $\delta \mathbf{B}$ is readily obtained using Comsol, and is shown in Fig.3. Importantly, we note that the B_1 field is essentially along $\mathbf{x}$ in the region just below the wire, and essentially along $\mathbf{y}$ in the region immediately outside of the wire. According to Eq.(5), one thus expects the coupling to the microwave field to be strongly θ-dependent for donors located immediately below the wire, and to depend negligibly on θ for those outside of the wire.

Sub-structures of the lines profiles

The spectroscopy of the transition $m_F = -5 \to m_F = -4$ was realized with the magnetic field B_0 applied successively along two directions : along $\mathbf{z}$ ($\theta = 0°$, parallel to the wire), and along $\mathbf{x}$ ($\theta = 90°$, perpendicular to the wire). As shown in Supplementary Figure 3, the low-field sub-peak appears only for $\theta = 0°$ whereas the upper-field structure remains unchanged for both orientations.

The profile of the microwave excitation field components B_{1x} and B_{1y} at a depth of $100\,\mathrm{nm}$ (implantation profile peak) is shown in Fig. 3d. As mentioned earlier the field below the wire is essentially along $\mathbf{x}$, whereas it is essentially along $\mathbf{y}$ outside the wire. When $\mathbf{B_0} = B_0\mathbf{z}$, B_1 is transverse to B_0 for all spins. When $\mathbf{B_0} = B_0\mathbf{x}$, B_1 is transverse to B_0 only

for spins outside the wire. This strongly suggests that when $\mathbf{B_0} = B_0\mathbf{z}$ both spin families can contribute to the signal and when $\mathbf{B_0} = B_0\mathbf{x}$ only spins outside the wire contribute.
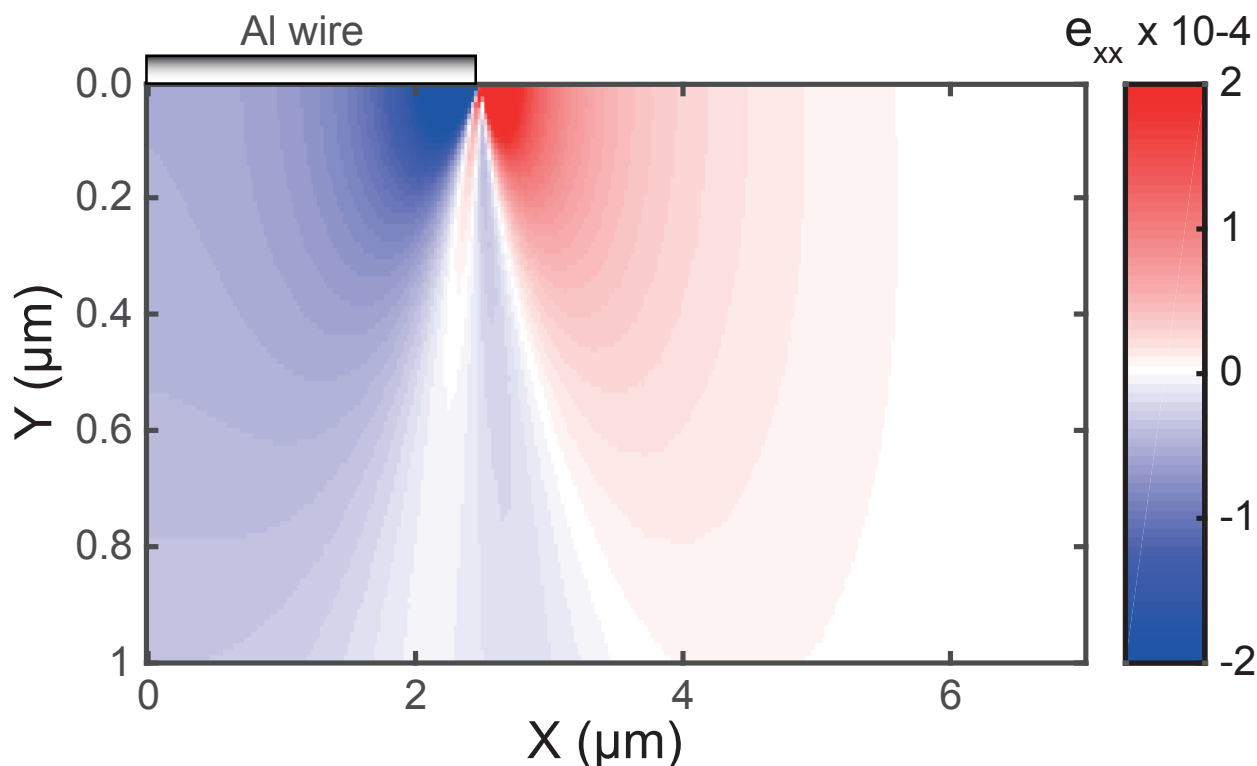
Supplementary Fig. 4. Diagonal strain tensor component ϵ_{xx} experienced by the donors as a result of thermal expansion coefficient mismatch between silicon and the aluminum LC resonator.

As a result of the larger thermal expansion coefficient for aluminium than for silicon, once cooled the region underneath the wire experiences a different strain to the region immediately outside of the wire see Supplementary Figure 4. Silicon is an indirect bandgap semiconductor with a six-fold degenerate conduction band minimum. The sharp confining potential of a donor causes the six-fold degenerate ground state to split into a singlet ground state: $A_1 = \frac{1}{\sqrt{6}}\{1,1,1,1,1,1\}$, a triply-degenerate excited state: $T_{2(x,y,z)} = \frac{1}{\sqrt{2}}\{1,-1,0,0,0,0\}, \frac{1}{\sqrt{2}}\{0,0,1,-1,0,0\}, \frac{1}{\sqrt{2}}\{0,0,0,0,1,-1\}$ and a doubly-degenerate excited state: $E_{(xy,xyz)} = \frac{1}{2}\{1,1,-1,-1,0,0\}, \frac{1}{\sqrt{12}}\{-1,-1,-1,-1,2,2\}$. Strain has the effect of lowering the energy of conduction band minima (or "valleys") in the direction of compressive strain and raising the energy of valleys in the direction of tensile strain. Each state will therefore have a shift in energy that depends on the applied strain and its valley composition [6]. In addition, strain mixes the ground state A_1 with the doublet excited states E_{xy}

and E_{xyz}.

The $I = 9/2$ nuclear spin of bismuth means that it possesses an electric quadrupole moment Q. The quadrupole moment can interact with an electric field gradient (EFG), which, for example, can be generated by the electron wavefunction through the operator [7]:

$$V_{\alpha\beta} = \langle \Psi | \widehat{H}_{\alpha\beta}^{\text{EFG}} | \Psi \rangle \tag{7}$$

$$\widehat{H}_{\alpha\beta}^{\text{EFG}} = \frac{e}{4\pi\epsilon} \frac{3\alpha\beta - r^2}{r^5} \tag{8}$$

where α or $\beta = x, y, z$ are the crystal or principal coordinate system. In the absence of strain, the ground state electron wavefunction is the A_1 state, which is a symmetric combination of the six valleys. This symmetric state produces no EFG and thus a vanishing quadrupole interaction (QI). On the other hand, the excited states are an asymmetric combination of valleys and result in an asymmetric charge distribution and a non-zero EFG. For the case of strain applied along the z principle axis, an EFG is produced through mixing with the doublet excited state E_{xyz}. The quadrupole coupling for a field B_0 applied in the direction of this EFG is given by the interaction Hamiltonian:

$$\widehat{H}_{\text{QI}} = eQV_{zz} \left(3\widehat{I}_z^2 - I(I+1) \right) / (4I(2I-1)) \tag{9}$$

From Equation (9), it is evident that the QI produces an energy shift only on transitions whose states have differing m_I. This is applicable to our low magnetic field transitions, which are highly mixed in the electron-nuclear basis. The sign of the EFG – and consequently the quadrupole shift of the spin transitions – depends on the sign of the induced strain, which as shown in Figure 4 is opposite for donors underneath the wire and to its side.

The measured spin resonance lines in our device are split above and below the theoretical field values (see Figure 2 of main manuscript), suggesting an underlying interaction with both positive and negative frequency components. As we have shown, such a frequency distribution could be explained by a strain-induced QI. This is completely consistent with the observation above that the two sub-peaks are subject to B_1 fields of different orientation. Spins constructing the high field peak experience a B_1 that is always perpendicular to B_0, which is true of spins to the side of the wire. Due to strain these spins see a different QI, which would explain such a shift in the resonance field. A quantitative comparison between theory and experiment is the subject of ongoing work.
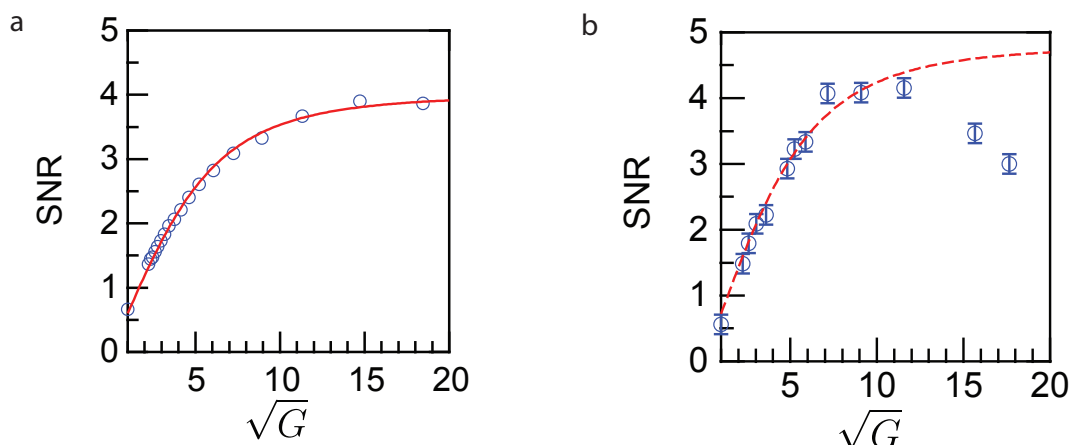
Supplementary Fig. 5. (a) Amplitude JPA signal-to-noise ratio $SNR = \sqrt{P_{out}/P_{noise}}$ as a function of $\sqrt{G}$ for an input microwave tone, measured with a Spectrum Analyzer, showing a six-fold improvement with the JPA on. The JPA is operated in the non-degenerate mode. Open blue circles are experimental data, red curve is a fit as explained in the text. (b) Echo signal-to-noise ratio (in amplitude) as a function of $\sqrt{G}$ (blue open circles), with error bars estimated as explained below. Red dashed line shows the amplifier $SNR(\sqrt{G})$ curve, rescaled to these data, showing that the spin-echo signal-to-noise is increased as expected from the JPA, until saturation.

III. EXPERIMENTAL DETERMINATION OF THE SIGNAL TO NOISE RATIO

We now discuss the experimental determination of the SNR. We first characterize the signal-to-noise ratio improvement brought by the JPA itself over the following HEMT amplifier cooled at $4\,\mathrm{K}$. A continuous microwave signal at frequency ω is sent directly on the JPA and its output spectrum P_{out} is measured with a spectrum analyzer for various JPA pump power settings in the non-degenerate mode. The JPA gain in the different setting may then be computed by $G = P_{out}/P_{out}(\mathrm{JPA\ off})$. The same experiment is then repeated without any input signal so as to obtain P_{noise}, the noise power in the measurement bandwidth of $100\,\mathrm{kHz}$. The amplitude signal-to-noise ratio is then evaluated by $SNR = \sqrt{P_{out}/P_{noise}}$ and is shown in Fig. 5a.

It follows the expected dependence $SNR \propto \sqrt{G/((G-1)n + n_{syst})}$, n being the total noise photon number with the JPA ON as defined in the main text, and n_{syst} being the number of noise photons added when the JPA is off. This yields a ratio $n_{syst}/n = 36$ as

observed in similar setups [8], indicating $n_{syst} \approx 36$ and $n_{amp} + n_{eq} \approx 1$ therefore approaching the quantum limit, with equal contributions from n_{eq} and n_{amp} (while $n_s \simeq 0.01n$ has a negligible contribution as verified experimentally).

We then study the SNR of the spin-echo at $B_0 = 5.18 \, \text{mT}$ for various JPA gains, using homodyne demodulation. For that we first choose the local oscillator phase such that the echo is entirely on one quadrature (I). We then average 10 spin-echo signals yielding time-traces $\bar{I}(t)$ from which we compute the integrated echo amplitude $\mathcal{S} = \frac{1}{T_E} \int_0^{T_E} \bar{I}(t)dt$, T_E being the echo duration; the noise is then obtained as $\mathcal{N} = \sqrt{\frac{1}{T_E} \int_0^{T_E} \bar{I}^2(t)dt}$ when the microwave pulses are off. The noise being determined with an averaging of 500 traces, the statistical uncertainty on the SNR comes from the signal, so that the absolute uncertainty $\epsilon_{SNR} = \epsilon_{\mathcal{S}}/\mathcal{N} = 1/\sqrt{10}$ since signal traces were averaged 10 times. As shown in Fig. 5, the resulting $SNR = \mathcal{S}/\mathcal{N}$ follows the same dependence as already obtained for the JPA itself, which shows that with the JPA on, the detected spin-echo reaches the quantum limit of sensitivity, with a gain in sensitivity by a factor $\times 7$ compared to JPA OFF.

It is possible to further improve the SNR by using the JPA in its degenerate mode, by setting $\omega_p = 2\omega_0$ and setting the relative phase of the pump tone such that the amplified quadrature is I. This increases the gain by $6 \, \text{dB}$ while only increasing the noise power by $3 \, \text{dB}$. The expected increase of SNR by $\sqrt{2}$ is indeed approximately observed, yielding a absolute signal-to-noise ratio of 7, a factor $\times 11$ larger than with the JPA OFF as shown in Fig.3 of the main text.

IV.   NUMERICAL SIMULATIONS

The goal of this section is to detail the numerical fits of the absorption and the spin-echo sequences shown in figure 3 of the main text. From this simulation, we extract the number of spins probed in a single spin-echo sequence as well as the measured spin concentration. In order to reproduce the spin dynamics, the inhomogeneity in both spin frequency and coupling strength is taken into account by dividing the ensemble into a sufficiently large set of homogeneous sub-ensembles and integrating the equations of motion for the resonator field and the spin components of all of the sub-ensembles using the model already described in[9–11].

Model

Consider an ensemble of N spin-1/2 particles of frequency ω_j. Each spin couples to the resonator field (described by creation and annihilation operators $\hat{a}^\dagger$ and $\hat{a}$) with a coupling constant g_j and a Jaynes-Cummings interaction (see Eq.4 above). The total system Hamiltonian is then

$$\hat{H}/\hbar = \omega_0 \hat{a}^\dagger \hat{a} + \frac{1}{2}\sum_{j=1}^{N}\omega_j\hat{\sigma}_z^{(j)} + i\sqrt{\kappa_1/2}(\beta\hat{a}^\dagger - \beta^*\hat{a}) + \sum_{j=1}^{N}(g_j^*\hat{\sigma}_+^{(j)}\hat{a} + g_j\hat{\sigma}_-^{(j)}\hat{a}^\dagger), \qquad (10)$$

with $\hat{\sigma}_k^{(j)}$ the Pauli operators of spin j for $k = \{+, -, z\}$, and β the amplitude of the microwave field driving the cavity input in the laboratory frame. The equations of motion are then integrated under the Markov approximation to incorporate the effect of resonator leakage and spin decoherence [11]. This numerical simulation yields the dynamical evolution of the mean values of the resonator field quadratures as well as of the spin operators.

The inhomogeneity in both spin resonance frequencies and coupling strengths is taken into account by dividing the entire inhomogeneous ensemble into M homogeneous sub-ensembles, $\mathcal{M}_1, \mathcal{M}_2, \ldots, \mathcal{M}_M$, each of them describing spins having an identical frequency ω_m and coupling to the cavity field g_m. For a sub-ensemble m, we define the total number of spins as N_m and the three spin collective operators as $\hat{S}_i^{(m)} = \sum_{j \in \mathcal{M}_m}\hat{\sigma}_i^{(j)}$, with $i \in \{x, y, z\}$.

Spin decoherence is treated by including a spin dephasing rate $\gamma_\perp = 1/T_2$ and a spin energy decay rate $\gamma_\parallel = 1/T_1$. We use the experimentally measured coherence time $T_2 = 9\,\mathrm{ms}$ (see Fig.2 of the main text). The energy relaxation rate on the other hand is dominated by Purcell relaxation through the cavity, meaning that T_1 is longer for spins detuned from the cavity than for spins perfectly at resonance as will be discussed in later work. This is captured by defining for each ensemble $\gamma_\parallel^{(m)}$ as $\kappa\frac{g_m^2}{\Delta_m^2 + \frac{\kappa^2}{4}}$, with $\Delta_m = \omega_m - \omega_0$. Note that the relaxation time shown in Figure 2 $T_1 = 0.4\,\mathrm{s}$ was taken with a very narrow bandwidth pulse so as to obtain only the contribution from the spins that are on resonance with the cavity.

This leads us to introduce for each sub-ensemble an effective initial polarisation $S_z^{(m)}(t = 0)$. Indeed, every experimental sequence is repeated several times at rate γ_{rep} ($\gamma_{rep}^{-1} \approx 3$ to 10s) and the results are then averaged. This waiting time γ_{rep}^{-1} is long enough compared to T_1 to be neglected for spins at resonance, however detuned spins have a longer T_1 and thus do not fully relax between two consecutive sequences, contributing less to the signal than

spins at resonance. To take into account this effect, we define an effective initial polarisation $S_z^{(m)}(t = 0)$ for a sub-ensemble depending on its relaxation time:

$$S_z^{(m)}(t = 0) = -N_m \times (1 - e^{-\gamma_{\|(m)}/\gamma_{rep}}) \tag{11}$$

The first step before performing the simulations is to determine in the context of the experiment the size N_m of each sub-ensemble, which requires knowledge of the distribution of coupling constants and resonance frequency within the spin-ensemble.

Determining the coupling constant distribution

From the simulation of the vacuum fluctuations of the magnetic field shown in Figure 3, one can compute the coupling constant distribution using Eq. 5. The measurements which we want to simulate were performed with the magnetic field B_0 aligned along the wire in the **z** direction, on the low-field peak of the structure shown on Figure 2, at 5.18 mT, attributed to spins lying under the wire. As a consequence, we compute the distribution only for this subset of spins, imposing $|x| < 2.5 \mu m$ and $\theta = 0$ in the formula. The inhomogeneous implantation profile of the spins is taken into account by appropriately weighing the coupling constant distribution. In order to normalize the distribution we take $\sum \rho(g_m) = 1$. As shown in Fig. 6a, this yields a very asymmetric distribution sharply peaked around $g/2\pi = 56$ Hz.

Determining the spin frequency distribution

The cavity linewidth (20 kHz) is two orders of magnitude smaller than the spin linewidth 3.25 MHz. In order to avoid numerical errors, we use a sampling of 1 bin per 1 kHz, over a range of 450 kHz. The zero order approximation would be to assume a square spin frequency distribution, nevertheless we introduce a tilted square distribution to take into account more precisely the shape of the line, Figure 6. The relative slope is derived from the observed spin-echo signal. At 5.18 mT, this yields a tilt of 10% on the chosen range.

Evaluating the number of spins

In order to determine the absolute scaling of the spin distributions, we measure the time-dependent absorption of the spins, as shown in Fig. 7. A first 500 μs-long pulse P of power
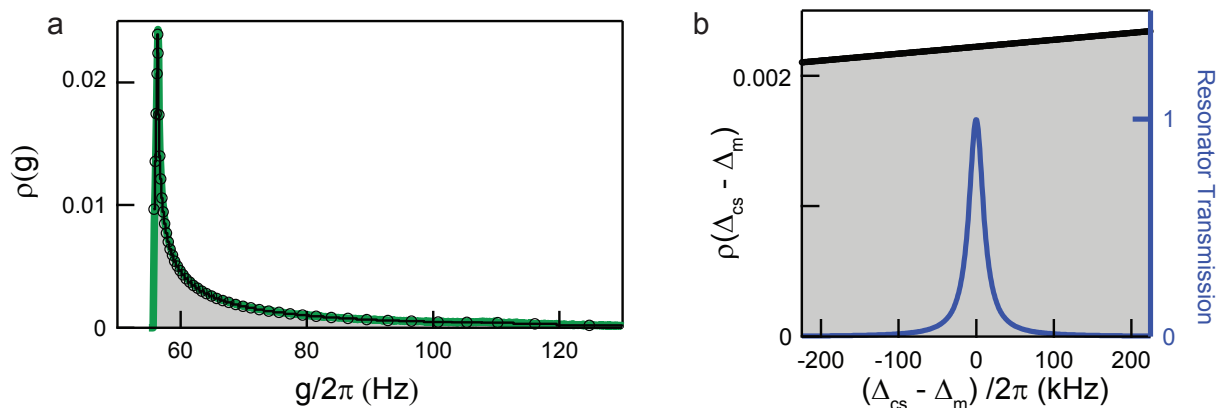
Supplementary Fig. 6. (a) Coupling strength distribution extracted from magnetic field simulation for $|x| < 2.5\,\mu$m, with $Z_0 = 44\Omega$, weighted by spin concentration and normalized to unity (green line). The black circles show the discrete distribution used in the simulation, with $M_g = 50$. (b) Tilted square distribution used in the simulation, with $M_{bins} = 450$ (black line). The resonator transmission is plotted for comparison (blue line)

P_{in} is sent to the unsaturated spins, leading to the absorption of the signal (Fig. 7c) whereas a second pulse of same power P_{in} sent immediately after a strong microwave pulse whose role is to saturate the spins shows only the cavity dynamics (subset b). The sequence is repeated 1000 times with a repetition time $\gamma_{rep}^{-1} = 3\,\text{s} = 10T_1$ to let the spins relax back to their ground state in-between the experimental sequences.

The transmitted pulse P shows two prominent features : the Rabi oscillation transients at the beginning, which are characterized by an oscillation frequency Ω_R, a decay time and an initial amplitude, and the free-induction decay (FID) of the spins which gives rise to the emission of a microwave signal even after the cavity field has decayed.

To simulate such a sequence, the coupling distribution and the spin frequency distribution detailed above have been scaled with a total number of spins $N_{tot} = \sum_m N_m$. The cavity parameters κ_1, κ_2, κ_L, and ω_c as well as spin relaxation rates $\gamma_\perp$ and $\gamma_\parallel$ are experimentally determined as explained earlier. The simulation of the saturated pulses transmission is in quantitative agreement with the data, without adjustable parameter (Figure 7b).

The simulated absorbed pulses are calculated with the same cavity parameters and an overall distribution scaling factor $N_{tot} = 2 \times 10^5$. This parameter gives a good agreement with the FID part of the signal as well as with the Rabi oscillations amplitude. To obtain the
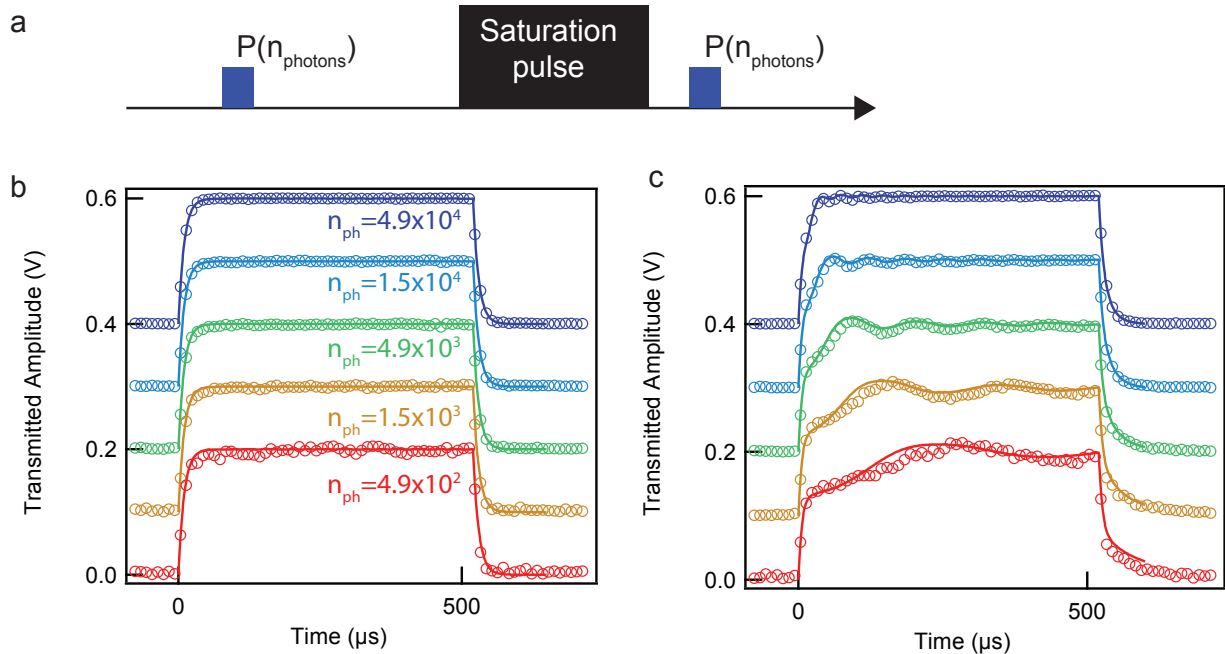
Supplementary Fig. 7. (a) Absorption sequence consisting of a first 500-us-long pulse at power P(nphotons), followed by a strong saturating microwave pulse immediately followed by a second 500-us-long pulse at same power P(nphotons). (b) Saturated pulses taken with average number of photons n_{ph} for the intra-cavity field, rescaled to same amplitude with an additional offset and averaged 1000 times. Open circles : data, solid lines : fit. (c) Absorbed pulses, for same n_{ph}, rescaled thanks to saturated curves and averaged 1000 times. Open circles : experimental data, solid lines: fit

right Rabi oscillation frequency, we simply need to scale by a factor $\eta = 1.1$ the power at the cavity input, compared to the input power estimated from the cables and filters attenuation. With only those two adjustable parameters, we are able to reproduce quantitatively the spin absorption (Figure 7c), which is a first validation for using this model as an evaluation of the number of spins contributing to the signal.

This approach neglects one aspect of the experiment. In our sample, the inhomogeneous broadening of the line is caused by strain due to the presence of the aluminium wire. One can thus expect a correlation between the frequency of a given spin and its coupling to the resonator. Taking this correlation between coupling constant and spin frequency into account quantitatively would however require a microscopic modelling for the strain which is not available so far. The excellent overall agreement between theory and measurements

indicates that the error is minor, although this approximation may account for the small discrepancy between simulated and experimental Rabi oscillations that can be noted for low powers in Figure 4c.

### Evaluating the number of spins contributing to the spin-echo signal

Having as explained above calibrated the absolute scale of the spin distribution, we now evaluate the number of spins involved in a spin-echo by simulating a full Hahn echo sequence, keeping exactly the same parameters for the spin distributions. The input power of the simulated $\pi/2$ and π pulses are calibrated by simulating Rabi oscillations. We find that in the simulation the π pulse power is only $1\,\mathsf{dB}$ away from the experimental one, which further confirms the validity of our model.

The spin echo sequence was acquired with the JPA off, in order to avoid its saturation by the drive pulses which would distort them. The output amplitude is scaled by comparing the theoretical and experimental decay of the two excitation pulses; with only this adjustment factor the simulated echo is found to be in quantitative agreement with the experimental data as shown in Fig.3 of the main text.

To evaluate the number of spins excited during the spin-echo sequence, we extract from the simulation the time-dependent mean spin polarization $\langle S_z \rangle$, as shown in Fig. 8a. We consider more particularly that the quantity $\langle S_z(t > \pi/2) \rangle - \langle S_z(t = 0) \rangle$ is a direct estimate of the number of spins excited by an Hahn-echo sequence. After the exponential decay of the $\pi/2$ excitation pulse, this value increases by 1.2×10^4. We thus come to the conclusion that 1.2×10^4 spins participate to the echo shown in Fig.3 of the main text, which is detected with a $SNR = 7$, which yields the sensitivity reported in the main text.

Evaluating the concentration of bismuth donor spins

Thanks to the determination of the spin density in absolute scale, we can compare the estimated number of spins to the known number of implanted atoms, to check that the two are consistent. We can scale the spin density $\rho(\omega_s) \propto A_e \times A_\pi$ thanks to the absorption simulation. By integrating the lower field peak, Figure 8b, we find a total number of spins of 1.07×10^6 contributing to the absorption. As Bismuth donors have a nuclear spin of 9/2, this
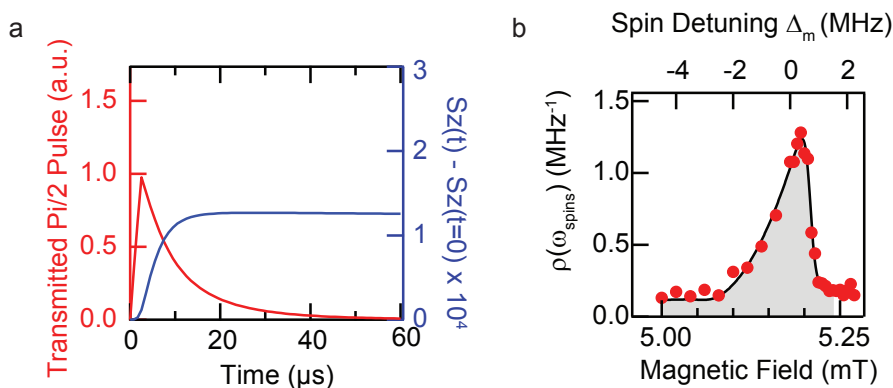
Supplementary Fig. 8. (a) Red: Simulated $\pi/2$ excitation pulse. Blue: $\langle S_z(t > \pi/2)\rangle - \langle S_z(t=0)\rangle$, allowing to extract 1.2×10^4 excited spins during this excitation pulse. (b) Spin density profile (red circles) $\propto A_e \times A_\pi$ (defined in the main text) rescaled to $\int \rho(\omega_{spins})d\omega_{spins} = 1$ (grey filled area).

represents only one-tenth of the total amount of spins. Also as this peak has been identified as signal emitted only by spins under the wire, the amount of spins is diluted in a surface $S_{wire} = L_{wire} \times W_{wire} = 720\mu m \times 5\mu m = 3.6 \times 10^{-5}\, cm^2$, leading to an experimental surface concentration $[Bi]_{Exp} = 10 \times 1.07 \times 10^6/(3.6 \times 10^{-5}) = 2.97 \times 10^{11}\, cm^{-2}$, a number which is only a factor 3 lower than the surface concentration extracted by SIMS measurement $[Bi]_{SIMS} = 9.45 \times 10^{11}\, cm^{-2}$.

This ratio of 30% can be explained by two factors: first that the activation of bismuth atoms i.e. the migration of bismuth atoms from interstitial implantation site to substitutional site by rapid annealing is not total. This factor has been evaluated in [1] to be 60% by electrical measurement. The additional factor 2 with our experiment may be due to a fraction of bismuth atoms being in an ionized state and thus not contributing to the ESR signal.

Approximate analytical formula for the expected spin-echo signal-to-noise ratio

We now derive an approximate analytical formula for the pulsed ESR spectrometer sensitivity, which is given in the main text. The goal is to provide an analytical estimate for the experimentally obtained sensitivity and thus identify how the sensitivity scales with the physical parameters.

Compared to the model used in section IV, we consider here for simplicity that all spins

have equal coupling constant g to the resonator. As a result in the frame rotating at the resonator frequency ω_0, the Hamiltonian is:

$$\hat{H}/\hbar = \sum_j \left[\frac{\Delta_j}{2} \hat{\sigma}_z^{(j)} + g(\hat{a}^\dagger \hat{\sigma}_-^{(j)} + \hat{a}\hat{\sigma}_+^{(j)}) \right]. \tag{12}$$

To obtain analytical results, it is convenient to assume that the spin detunings Δ_j are distributed according to a Lorentzian function $f(\Delta) = \frac{w/2\pi}{\Delta^2 + w^2/4}$, with a FWHM of w. More realistic distributions would only change the final results by a factor of order unity. For simplicity again, we neglect decoherence of the spins. The following equations of motion then describe the evolution of mean values:

$$\frac{d\langle \hat{a}(t) \rangle}{dt} = -\frac{\kappa}{2} \langle \hat{a}(t) \rangle - ig \sum_j \langle \hat{\sigma}_-^{(j)}(t) \rangle, \tag{13}$$

$$\frac{d\langle \hat{\sigma}_-^{(j)}(t) \rangle}{dt} = -i\Delta_j \langle \hat{\sigma}_-^{(j)}(t) \rangle + ig \langle \hat{\sigma}_z^{(j)}(t)\hat{a}(t) \rangle \tag{14}$$

We define $\hat{S}_- = \sum_j \hat{\sigma}_-^{(j)}$, and formally integrate (13),

$$\langle \hat{a}(t) \rangle = -ig \int_{-\infty}^t e^{-\frac{\kappa}{2}(t-t')} \langle \hat{S}_-(t') \rangle dt'. \tag{15}$$

From this equation we see that $\langle \hat{a} \rangle$ attains at most a value of $\approx gN/\kappa$, and if g times this value is much smaller than typical detunings, Δ_j, i.e., the cooperativity parameter $C = \frac{4g^2 N}{\kappa w} \ll 1$, the second term of Eq. (14) can be neglected. We assume this is the case and we thus treat the spins as evolving freely between the pulses.

We will focus on the case of a standard Hahn-echo sequence, $\pi/2-\tau-\pi-\tau$, and we assume perfect initial $\pi/2$ and refocusing π pulses at times -2τ and $-\tau$, respectively. Prior to $t = -2\tau$, the spins are polarized with polarization $p \le 1$ along the $-z$-direction such that $\langle \hat{\sigma}_z^{(j)} \rangle = -p$ and $\langle \hat{\sigma}_x^{(j)} \rangle = \langle \hat{\sigma}_y^{(j)} \rangle = 0$. The case $p = 1$ corresponds to a perfectly polarized sample with all spins in the ground state. When the spin ensemble is subjected to the perfect $\pi/2$ pulse around the x-axis at time $t = -2\tau$, a state with $\langle \hat{\sigma}_y^{(j)}(0) \rangle = p$ and hence $\langle \hat{\sigma}_-^{(j)}(0) \rangle = -\frac{ip}{2}$ is prepared. The refocusing π pulse at $t = -\tau$ implies that a spin echo will occur at time $t = 0$, where the free evolution, $\langle \hat{\sigma}_-^{(j)}(t) \rangle = -\frac{ipe^{-i\Delta_j t}}{2}$, cause all spins to be in phase. The resulting total spin $\langle \hat{S}_-(t) \rangle$ can be calculated in the continuum limit, where the sum over spins is replaced by an integral over detunings,

$$\langle \hat{S}_-(t) \rangle = \int f(\Delta) \frac{-ipN}{2} e^{-i\Delta t} d\Delta = -\frac{ipN}{2} e^{-w|t|/2}. \tag{16}$$

Inserting this into Eq. (15) leads to the following time dependence of the resonator field:

$$\langle \hat{a}(t) \rangle = -\frac{gpN}{\kappa + w} \times \begin{cases} e^{\frac{wt}{2}} & t < 0, \\ \frac{\kappa + w}{\kappa - w} e^{-\frac{wt}{2}} - \frac{2w}{\kappa - w} e^{-\frac{\kappa t}{2}} & t > 0. \end{cases} \qquad (17)$$

Now, as indicated in Fig. (1) of the main text, this resonator field is coupled with rate κ_2 into a Josephson parametric amplifier (JPA). The input field, $\hat{a}_{\mathrm{in}}$, to this amplifier is related to the resonator field, $\hat{a}$, by $\langle \hat{a}_{\mathrm{in}}(t) \rangle = \sqrt{\kappa_2} \langle \hat{a}(t) \rangle$ and is normalized such that $\langle \hat{a}_{\mathrm{in}}^{\dagger}(t) \hat{a}_{\mathrm{in}}(t) \rangle$ represents the number of microwave photons per time incident on the amplifier. We shall also define the input field quadrature variables by $\hat{X}_{\mathrm{in}}(t) = \frac{\hat{a}_{\mathrm{in}}(t) + \hat{a}_{\mathrm{in}}^{\dagger}(t)}{2}$ and $\hat{Y}_{\mathrm{in}}(t) = \frac{-i(\hat{a}_{\mathrm{in}}(t) - \hat{a}_{\mathrm{in}}^{\dagger}(t))}{2}$. Since $\langle \hat{a}(t) \rangle$ is real-valued in our calculations, see Eq. (17), the mean signal is carried by the $\hat{X}$-quadrature.

So far we have only considered mean values of the spins and the cavity field, and we shall apply an operator description of the amplification stage to assess the noise on the measurement signal. To this end we define single modes of the propagating field by $\hat{a}_{\mathrm{in}} = \int \hat{a}_{\mathrm{in}}(t) u(t) dt$, where $u(t)$ is a mode function chosen to be real valued and fulfilling $\int [u(t)]^2 dt = 1$. In this case we have $[\hat{a}_{\mathrm{in}}, \hat{a}_{\mathrm{in}}^{\dagger}] = \iint u(t) u(t') [\hat{a}_{\mathrm{in}}(t), \hat{a}_{\mathrm{in}}^{\dagger}(t')] dt dt' = 1$ due to the free field commutator relations $[\hat{a}_{\mathrm{in}}(t), \hat{a}_{\mathrm{in}}(t')] = \delta(t - t')$. The corresponding single mode quadrature variables, $\hat{X}_{\mathrm{in}} = \int \hat{X}_{\mathrm{in}}(t) u(t) dt$ and $\hat{Y}_{\mathrm{in}} = \int \hat{Y}_{\mathrm{in}}(t) u(t) dt$, fulfill $[\hat{X}_{\mathrm{in}}, \hat{Y}_{\mathrm{in}}] = \frac{i}{2}$, and the minimum uncertainty state, obtained for the vacuum state or coherent states of the field, must obey $\langle \Delta \hat{X}_{\mathrm{in}}^2 \rangle = \langle \Delta \hat{Y}_{\mathrm{in}}^2 \rangle = \frac{1}{4}$.

Noise in the propagating field is conveniently characterized by its dimensionless power spectrum $S(\omega)/\hbar\omega = \langle \Delta \hat{X}_{\mathrm{in}}^2 + \Delta \hat{Y}_{\mathrm{in}}^2 \rangle$. At the cavity output, noise arises from both electromagnetic equilibrium fluctuations, characterized by n_{eq}, and from possible extra noise due to spontaneous emission of the spins, as will be discussed further, with a contribution n_{sp}. Our experiments being performed at temperatures such that $kT \ll \hbar\omega_0$, the electromagnetic field at equilibrium is indeed very close to its ground state so that we can safely assume that $n_{\mathrm{eq}} = 1/2$. In total we get $\langle \Delta \hat{X}_{\mathrm{in}}^2 \rangle = \frac{1}{2}(n_{\mathrm{sp}} + \frac{1}{2})$.

When the signal pulse, emitted from the resonator, is transmitted through the amplifier, its power is increased by the gain G. However the amplification process itself can add extra noise to the output field, characterized by a dimensionless power density n_{amp}, and further degrade the signal-to-noise ratio. Following Caves [12], two cases should then be envisioned to describe the statistics of the field at the amplifier output. If the amplifier is in the so-called non-degenerate mode, its single mode output is described by the field annihilation

operator:

$$\hat{a}_{\mathrm{out}} = \sqrt{G}\, \hat{a}_{\mathrm{in}} + \sqrt{G-1}\, \hat{b}_{\mathrm{id}}^{\dagger}. \tag{18}$$

To ensure the bosonic commutator relation of the amplified signal operators, an idler mode operator, obeying $[\hat{b}_{\mathrm{id}}, \hat{b}_{\mathrm{id}}^{\dagger}] = 1$, must be included in the amplifier relation [12]. It should also be noted that the gain G is generally a function of frequency, which may distort the temporal shape of an amplified pulse. However, the measured 1.7 MHz wide gain profile, see Fig. 1(f) of the main text, supports that we can assume a constant gain across the bandwidth of the signal and hence for the single mode defined by $u(t)$.

We introduce quadrature operators for the output and idler modes in a similar manner as for the input field, and the mean value of the input field is simply amplified as $\langle \hat{X}_{\mathrm{out}} \rangle = \sqrt{G} \langle \hat{X}_{\mathrm{in}} \rangle$. However, the noise in the output has contributions from both the signal and the idler mode,

$$\langle \Delta \hat{X}_{\mathrm{out}}^2 \rangle = G \langle \Delta \hat{X}_{\mathrm{in}}^2 \rangle + (G-1)\langle \Delta \hat{X}_{\mathrm{id}}^2 \rangle. \tag{19}$$

Assuming the idler mode thermalized at a temperature T yields $\langle \Delta \hat{X}_{\mathrm{id}}^2 \rangle = \frac{1}{4}(1 + 2\bar{n})$, $\bar{n} = 1/(\mathrm{e}^{\frac{\hbar \omega_0}{kT}} - 1)$ being the mean thermal photon number. At high temperatures $\frac{k_{\mathrm{B}}T}{\hbar \omega_0} \gg 1$ so that $\bar{n} \simeq \frac{k_{\mathrm{B}}T}{\hbar \omega_0}$, the thermal state of the idler yields an overwhelming contribution $(G-1)\frac{n_{\mathrm{amp}}}{2}$ to the readout noise on the X quadrature, with $n_{\mathrm{amp}} = \bar{n}$. This is in particular the case in our experiments when the JPA is turned off and the signal is exclusively amplified by the HEMT amplifier at the 4K stage, for which $n_{\mathrm{amp}} \sim 50$. When the JPA is on, this contribution is minimized since amplification is now carried on at a temperature T such that $k_{\mathrm{B}}T \ll \hbar \omega_0$, with an amplifier that reaches the quantum limit. In these conditions, $n_{\mathrm{amp}} = 1/2$.

In total, we find that the amplification obeys the following relation for the signal-to-noise ratio :

$$\frac{\langle \hat{X}_{\mathrm{out}} \rangle^2 / \Delta \hat{X}_{\mathrm{out}}^2}{\langle \hat{X}_{\mathrm{in}} \rangle^2 / \Delta \hat{X}_{\mathrm{in}}^2} = \frac{G(n_{\mathrm{eq}} + n_{\mathrm{sp}})}{G(n_{\mathrm{eq}} + n_{\mathrm{sp}}) + (G-1)n_{\mathrm{amp}}}. \tag{20}$$

In the special case that $n_{\mathrm{amp}} = n_{\mathrm{eq}} = \frac{1}{2}$ and assuming $n_{\mathrm{sp}} = 0$, this equals $\frac{G}{2G-1}$, which yields, in the limit of large G, the well known factor of two (i.e. 3 dB) reduction in squared signal-to-noise by phase insensitive amplification with no excess noise. After amplification by the JPA, the signal level is sufficient that amplification and homodyne demodulation do not further degrade the signal-to-noise. In our analytical estimate of the ESR sensitivity, we shall proceed with the assumption that the temperature is sufficiently low, the gain

is sufficiently high, and the excess spin noise is negligible (we shall return briefly to an assessment of this assumption).

The other case to consider is the one where the amplifier is phase-sensitive, with quadrature-dependent gains $G_{X,Y}$. This ensures the correct output commutator relations without requiring the addition of idler mode noise as explained in [12]. An ideal amplifier at the quantum limit may then verify $G_X = G_Y^{-1} \gg 1$ while implementing noiseless amplification of one of the two quadratures, implying that in this case $\langle \Delta \hat{X}_{\text{out}}^2 \rangle = n/2$, with $n = n_{\text{eq},X} + n_{\text{amp},X}$ and $n_{\text{amp},X} = 0$.

Summing up the discussion, one sees that the noise on quadrature X referred to the JPA input can be written as $\langle \Delta \hat{X}_{\text{out}}^2 \rangle = n/2$, with $n = n_{\text{eq}} + n_{\text{amp}} + n_{\text{sp}}$. In our experiment, $n_{\text{eq}} \sim 1/2$, whereas $n_{\text{amp}} \sim 50$ if the JPA is off, $n_{\text{amp}} \sim 1/2$ if it is operated in the non-degenerate mode, and $n_{\text{amp}} \sim 0$ if it is operated in degenerate mode.

Eqs. (19, 20) account for the noise and signal-to-noise for measurements of the continuous output amplitude signal weighted with $u(t)$. The optimal choice for $u(t)$ is the one that maximizes the weighted signal $\langle \hat{X}_{\text{out}} \rangle$ without altering the noise (assuming uniform broad band noise of the idler mode $\hat{b}_{\text{id}}$). In an experiment one may choose $u(t)$ as the measured shape of the emitted pulse averaged over many experimental runs. As shown by the red curve in the inset of Fig. 3(c) in the main text, we can obtain the same shape by a numerical calculation of the spin dynamics. Since we are here interested in analytical estimates, we choose the result given by $u(t) = \langle \hat{X}_{\text{in}}(t) \rangle / \langle \hat{X}_{\text{in}} \rangle$, where $\langle \hat{X}_{\text{in}}(t) \rangle = \frac{1}{2} \langle \hat{a}_{\text{in}}(t) + \hat{a}_{\text{in}}^\dagger(t) \rangle = \frac{\sqrt{\kappa_2}}{2} \langle \hat{a}(t) + \hat{a}^\dagger(t) \rangle = \sqrt{\kappa_2} \langle \hat{a}(t) \rangle$, with an explicit expression given in Eq.(17). To obtain the correct normalization $\int [u(t)]^2 dt = 1$, we calculate the squared signal as:

$$\langle \hat{X}_{\text{in}} \rangle^2 = \int \langle \hat{X}_{\text{in}}(t) \rangle^2 dt = \frac{2g^2 p^2 N^2 \kappa_2 (\kappa + 2w)}{(\kappa + w)^2 w \kappa}. \tag{21}$$

The output signal-to-noise ratio then reads:

$$\frac{|\langle \hat{X}_{\text{out}} \rangle|}{\Delta \hat{X}_{\text{out}}} = \frac{2gpN}{\kappa + w} \sqrt{\frac{1}{n}} \sqrt{\frac{\kappa_2 (\kappa + 2w)}{w\kappa}}. \tag{22}$$

The minimum number of detectable spins, which defines the ESR spectrometer sensitivity, is thus

$$N_{\text{min}} = \frac{\kappa + w}{2gp} \sqrt{\frac{nw\kappa}{\kappa_2 (\kappa + 2w)}} \rightarrow \frac{\kappa}{2gp} \sqrt{\frac{nw}{\kappa_2}}. \tag{23}$$

The arrow indicates the limit of conventional ESR operation, $\kappa \gg w$. Introducing the echo duration $T_E = w^{-1}$ as seen from Eq. 17, and taking the case of a critically coupled resonator

for which $\kappa = 2\kappa_2$, one obtains $N_{\min} = \frac{1}{gp}\sqrt{\frac{\kappa n}{T_E}}$, which is the formula found in the main text in the experimentally relevant case $p = 1$. For our parameters, this yields $N_{min} = 400$.

This estimate can be further refined to take into account the fact that the actual width $\Gamma/2\pi \approx 1$ MHz of the spin frequency distribution is much larger than κ. In this case, the $\pi/2$ and π pulses excite a subset of spins, and according to the numerical simulations, this subset has a Lorentzian profile with $w/2\pi \approx 25$ kHz, which is very close to $\kappa/2\pi \approx 22$ kHz. Hence, in the above expression (to the left of the arrow) one can take $\kappa \approx w \approx 2\kappa_2$ for critical coupling, which yields $N_{\min} \approx \sqrt{\frac{2}{3}}\frac{\kappa\sqrt{n}}{g} \approx 3\cdot 10^2$, using $g/2\pi \approx 55$ Hz and $p \approx 1$. This refinement should however not be considered too seriously when compared to the experimental data, given the other approximations that were made, such as perfect π pulse, Lorentzian line profile, and optimal weighing function $u(t)$.

The signal is further enhanced, with no increase in the noise, when accumulated over the CPMG echoes, i.e., by choosing the corresponding multi-peaked $u(t)$, cf. Fig. 4(a) of the main text. In the analysis of the experiments, we assumed a weighting of the signals by tophat pulses of equal weight, and we, indeed, observed an improved signal-to-noise over the single pulse analysis. Let us here estimate the theoretical limitations of the CPMG echo spectroscopy, assuming a gradual, exponential reduction of the echo amplitudes. With m pulses in total, we may define the corresponding normalized mode function $u^{(m)}(t)$ implicitly as:

$$u^{(m)}(t) = \frac{\sum_{j=0}^{m-1}\langle \hat{X}_{\text{in}}^{(1)}(t - jT)\rangle e^{-jT/T_{CPMG}}}{\langle \hat{X}_{\text{in}}^{(m)}\rangle}, \tag{24}$$

where $\langle \hat{X}_{\text{in}}^{(1)}(t)\rangle$ is the output quadrature for a single π pulse and we assume that the echoes are non-overlapping and simply repeated with a period of T but damped by the rate T_{CPMG}^{-1}. This T_{CPMG} may include any experimentally determined damping effects, such as non-ideal π pulses causing a degradation of the signal. As in the above analysis, the normalization, $\int[u^{(m)}(t)]^2 dt = 1$ is automatically accounted for when calculating the squared signal as:

$$\langle \hat{X}_{\text{in}}^{(m)}\rangle^2 = \int \sum_{j=0}^{m-1}\langle \hat{X}_{\text{in}}^{(1)}(t - jT)\rangle^2 e^{-2jT/T_{CPMG}} dt = \langle \hat{X}_{\text{in}}^{(1)}\rangle^2 \frac{1 - e^{-2mT/T_{CPMG}}}{1 - e^{-2T/T_{CPMG}}}. \tag{25}$$

The use of multiple pulses in the CPMG protocol only makes sense if $T \ll T_{CPMG}$, and the denominator in the above expression can be approximated as $2T/T_{CPMG}$. Hence, the

signal-to-noise ratio, SNR_m for m pulses becomes:

$$\frac{\text{SNR}_m}{\text{SNR}_1} = \sqrt{\frac{T_{CPMG}}{2T}(1 - e^{-2mT/T_{CPMG}})}, \qquad (26)$$

which behaves as $\sqrt{m}$ for a small number of pulses with $2mT \ll T_{CPMG}$ and saturates at $\sqrt{T_{CPMG}/2T}$ when $2mT \gg T_{CPMG}$.

Let us finally return to our assumption that the spin noise is negligible. To assess this issue we have performed a numerical calculation similar to the one shown in Fig. 3(c) in the main text, but including also the quantum noise using the methods of [9]. For an effective number of spins $N \approx 1.2 \cdot 10^4$, this calculation, indeed, shows an excess noise of ≈ 30 %, and we find that this noise is proportional to the number of spins involved. Since the excess noise is calculated for the situation where the signal-to-noise ratio is 7 ± 1, it must be seven times smaller, i.e., only at a few percent level when the signal-to-noise is unity. For this reason, it does not affect the experimental assessment of $N_{\text{min}} \approx 1.7 \cdot 10^3$ in the main text. We also note that with the effective number of spins $N \approx 1.2 \cdot 10^4$, the cooperativity parameter reaches the value of $C = \frac{4g^2 N}{\kappa w} \approx 0.26$. This number is also proportional to N and thus approximately seven times smaller in the case of a signal-to-noise level of unity, thus validating our assumption, $C \ll 1$, in the analytical estimate.

[1] C. D. Weis, C. C. Lo, V. Lang, A. M. Tyryshkin, R. E. George, K. M. Yu, J. Bokor, S. A. Lyon, J. J. L. Morton, and T. Schenkel, "Electrical activation and electron spin resonance measurements of implanted bismuth in isotopically enriched silicon-28," Applied Physics Letters **100**, 172104 (2012).

[2] A. Palacios-Laloy, *Superconducting qubit in a resonator : test of the Leggett-Garg inequality and single-shot readout* (PhD Thesis, 2010).

[3] X. Zhou, V. Schmitt, P. Bertet, D. Vion, W. Wustmann, V. Shumeiko, and D. Esteve, "High-gain weakly nonlinear flux-modulated josephson parametric amplifier using a squid array," Phys. Rev. B **89**, 214517 (2014).

[4] Gary Wolfowicz, Alexei M Tyryshkin, Richard E George, Helge Riemann, Nikolai V Abrosimov, Peter Becker, Hans-Joachim Pohl, Mike LW Thewalt, Stephen A Lyon, and John JL Morton, "Atomic clock transitions in silicon-based spin qubits," Nature nanotechnology **8**, 561–564 (2013).

[5] T. Van Duzer and C. Turner, *Superconductive Devices and Circuits* (Prentice Hall PTR, 1999).

[6] M. Usman, C. D. Hill, R. Rahman, G. Klimeck, M. Y. Simmons, S. Rogge, and L. C. L. Hollenberg, "Strain and electric field control of hyperfine interactions for donor spin qubits in silicon," Phys. Rev. B **91**, 245209 (2015).

[7] C. Slichter, *Principles of Magnetic Resonance* (Springer Ed., 1990).

[8] M.A. Castellanos-Beltran, K.D. Irwin, G.C. Hilton, L.R. Vale, and K.W. Lehnert, "Amplification and squeezing of quantum noise with a tunable josephson metamaterial," Nature Physics **4**, 929–931 (2008).

[9] B. Julsgaard and K. Mølmer, "Reflectivity and transmissivity of a cavity coupled to two-level systems: Coherence properties and the influence of phase decay," Phys. Rev. A **85**, 013844 (2012).

[10] B. Julsgaard, C. Grezes, P. Bertet, and K. Mølmer, "Quantum memory for microwave photons in an inhomogeneously broadened spin ensemble," Phys. Rev. Lett. **110**, 250503 (2013).

[11] C. Grezes, B. Julsgaard, Y. Kubo, M. Stern, T. Umeda, J. Isoya, H. Sumiya, S. Abe, S. Onoda, T. Ohshima, V. Jacques, J. Esteve, D. Vion, D. Esteve, K. Moelmer, and P. Bertet, "Multimode storage and retrieval of microwave fields in a spin ensemble," Phys. Rev. X **4**, 021049 (2014).

[12] Carlton M. Caves, "Quantum limits on noise in linear amplifiers," Phys. Rev. D **26**, 1817–1839 (1982).